

<https://doi.org/10.1038/s43247-024-01549-7>

Extreme summer temperature anomalies over Greenland largely result from clear-sky radiation and circulation anomalies



Manuel Tobias Blau ^{1,2}, Kyung-Ja Ha ^{1,2,3,4} ✉ & Eui-Seok Chung ⁵ ✉

The polar regions have been undergoing amplified warming in recent years. In particular, Greenland has experienced anomalously warm summers with intense melt rates. We employ a surface radiation budget framework to examine the causes for positive and negative summer temperature anomaly events over Greenland from 1979 to 2021. We found a dominant contribution of the clear-sky downwelling longwave radiation and the surface albedo feedback to temperature anomalies. Atmospheric temperature perturbations dominate the effect of anomalous emissivity on clear-sky downwelling longwave radiation. In warm years, enhanced turbulent heat exchange due to increased surface temperature and diabatic warming in the troposphere induces adiabatic heating of the atmosphere, enhanced moisture advection, and a high-pressure anomaly with a blocking-like anti-cyclonic circulation anomaly following peak temperature days. Different modes of natural climate variability, in particular, related to blocking over Greenland, can further amplify or dampen the ongoing warming trend, causing extreme temperature events.

Arctic temperatures exhibit a distinct seasonality due to the annual migration of solar zenith position characterized by polar night during boreal winter and polar day during boreal summer. Only during summer, does the mean temperature exceed the freezing point and result in snow, ice sheet, and glacier melting of varying intensity^{1–4}. Previous studies related enhanced snow and ice sheet melting over Greenland to anomalous warm air advection associated with high-pressure blocking conditions and intensified anticyclonic circulation^{4–10}. For instance, the most recent melt events in 2012 were linked to above-normal temperatures near the surface and in the troposphere, resulting in intense melting, while in 2019, a below-normal snowfall resulted in a negative surface mass balance⁹. Also, ocean heat transport and stratification can enhance melting in the ablation zone. For instance, ocean water from the Atlantic can submerge the Polar water, reducing the stratification and enhancing heat transport towards the ice and glacier margins¹¹. The ocean contribution was most distinct in the south of Greenland, while in the north of Greenland, the glacier melting was more sensitive to atmospheric warming¹². For instance, Mattingly et al.¹³ discussed the role of foehn wind-fashion downslope winds in enhancing the ice melt of northeast Greenland via surface and atmospheric warming. These foehn winds were related to atmospheric rivers embedded in southerly anomalies descending towards the coast, warming the surface and the lower- and mid-troposphere¹³.

Over the past several decades, significant trends have been observed in the Arctic. The ice sheet has undergone a significant negative trend in terms of mass balance^{14,15}. Further, there is a significant warming that exceeds the corresponding global average affecting the Arctic, including Greenland. This enhanced warming in the northern polar regions is referred to as Arctic Amplification^{10,15–25}. This warming trend was attributed to local feedback processes^{26–30}, especially lapse-rate feedback, the heat release from the Arctic Ocean^{16,18,26,31}, and energy transport from lower latitudes^{17,27}. Previous studies also indicated that melting sea ice during summer has increased the ocean heat storage via surface albedo feedback, which has been released to the atmosphere during the cold season^{17,18,21,27}. Further, the decreasing trend of sea ice and the Greenland ice sheet resulted in a growing importance of cloud feedback processes, as clouds acted as the primary reflector for incoming solar radiation with decreasing ice²². Another study pointed out that the latent heat exchange between the surface and the atmosphere contributed to Arctic amplification on a timescale of less than a month, while the surface albedo feedback played an important role on longer timescales²³.

The Greenland region has experienced substantial year-to-year variability in association with climate modes. First, the North Atlantic oscillation, which describes changes in the pressure gradient over the North Atlantic with Iceland in the north (low pressure) and the Azores in the south

¹Center for Climate Physics, Institute of Basic Sciences, Busan, South Korea. ²Department of Climate System, Pusan National University, Busan, South Korea.

³BK21 School of Earth and Environmental Systems, Pusan National University, Busan, South Korea. ⁴Institute for Future Earth, Pusan National University, Busan, South Korea. ⁵Division of Atmospheric Sciences, Korea Polar Research Institute, Incheon, South Korea. ✉ e-mail: kjha@pusan.ac.kr; echung@kopri.re.kr

(high pressure)^{32,33}, was negatively correlated with Greenland temperature and precipitation^{32,34–36}. The Greenland blocking index is a second mode, which is anti-correlated with the North Atlantic oscillation. The Greenland blocking index, which indicates the strength and frequency of high-pressure blocking conditions over Greenland, was positively correlated with Greenland temperature^{10,33,35,37–41}. Both modes have exerted a substantial impact on the strength and position of the jet stream by increasing the westerly component, reducing the advection of warm and moist air towards Greenland in a positive phase of the North Atlantic oscillation (negative Greenland blocking index)^{19,32,33}. Also, the East Atlantic pattern has shown a positive correlation with Greenland temperature^{35,42–44}. Other indices of climate variability that exerted teleconnections to Greenland climate conditions include the Scandinavian pattern⁴³, the Arctic oscillation⁴⁵, the East Atlantic/West Russia pattern⁴², the East Pacific/North Pacific pattern⁴², the Pacific North America pattern⁴⁶, the Quasi-biennial oscillation⁴⁷, the El Niño–Southern Oscillation⁴⁸, and the Atlantic multi-decadal oscillation⁴⁹.

The Greenland blocking index is an indicator for the frequency and intensity of blocking over Greenland^{10,37,40,50}. Blocking events, characterized by anomalous anti-cyclonic circulation, wave breaking at the jet stream, and subsidence^{10,41,51–53}, are an important factor affecting regional weather and climate extremes, such as droughts and extreme rainfalls^{50,51}. Also, extreme hot and cold temperature anomalies can occur due to blocking and associated cut-off anti-cyclones^{4,40,50,53}. Further, Preece et al.⁴¹ elaborated that heat extremes associated with omega-blocking systems favor the decline of the Greenland ice sheet; for instance, a cut-off anti-cyclone over Greenland was identified as the driving force for enhanced ice sheet melting in 2015⁴. Also, climate variability on interannual or decadal timescale can, to some extent, be related to blocking, with regional effects depending on the location of the blocking system along with the jet stream⁵⁴. Previous studies showed that blocking systems can develop over various regions in the North Atlantic and Europe, including east Greenland. For instance, snow cover anomalies in North America can cause a wavier jet stream and blocking, as a stationary Rossby wave

response¹⁰. The blocking anti-cyclones over east Greenland have been most relevant for warm anomalies over Greenland^{10,41,50,55}.

In this study, we elucidate processes causing extreme temperature anomalies from the perspective of the atmosphere, energy balance processes, and natural variability. Previously, various energy balance decomposition methods have been employed to attribute Arctic and Greenland warming to different radiative processes^{16–18,26–30}. However, a detailed decomposition has rarely been applied to extreme temperature events on inter-annual time scales. Therefore, in this study, we focus on year-to-year perturbations of the surface energy budget to explain Greenland's extreme temperature from 1979 to 2021.

Our target is to elaborate on the effects of radiative and non-radiative energy perturbations on temperature over Greenland in terms of trends and inter-annual extremes. Further, we explore atmospheric anomalies leading to extreme temperatures and how they explain the deviations of the radiation budget at the surface. Finally, we aim to create a global context by elaborating on the effect of different modes of variability influencing regional climate over Greenland.

Results

Greenland surface temperature anomalies

We used a surface energy budget framework to attribute anomalies relative to the 1979–2021 period and trends in the surface temperature over the Greenland domain (60–85°N, 75–15°W; Figs. 1 and 2a, black box)²⁹. This approach allows us to subdivide the temperature perturbations into partial temperature contributions of radiative and non-radiative terms of the surface energy budget. Radiative processes include the surface albedo feedback (SAF), the cloud radiative effect (CRE), the effect of changes in net shortwave radiation under clear-sky conditions (SWCS), and the effect of changes in the downwelling longwave radiation under clear-sky conditions (LWCS). Therefore, the effect of clear-sky downwelling longwave radiation on surface temperature anomalies combines the radiative effect of changes in the atmospheric temperature and the effect of changes in the emissivity

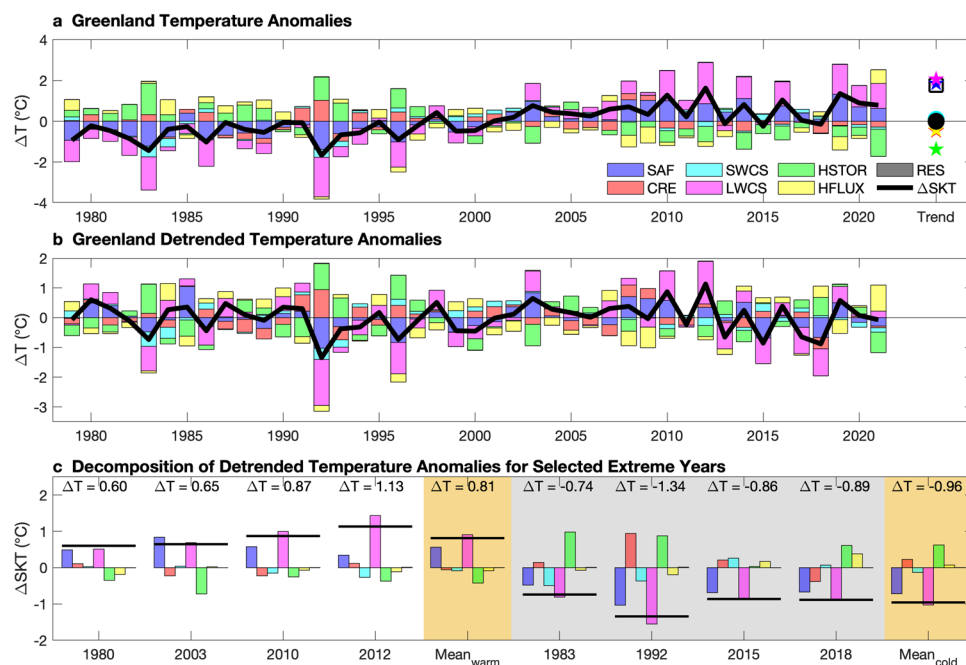


Fig. 1 | Attribution of summer temperature anomalies to surface energy budget perturbations. The figure illustrates the total (a) and detrended (b) summer surface temperature anomalies over Greenland and relates those to perturbations in the surface energy budget. Further, panel c shows detrended temperature anomalies for extreme cases. The attribution to surface energy budget perturbations includes the effect of the surface albedo (SAF), the effect of clouds on radiative fluxes (CRE), the effect of anomalous shortwave and longwave radiation under the clear-sky

assumption (SWCS and LWCS), the effect of changing heat storage (HSTOR), and the effect of changing turbulent heat fluxes (HFLUX). Total anomalies in a are relative to the 1979–2021 baseline period. The digits in c show the detrended temperature anomalies in the respective years. The gray shading highlights the below-normal temperature anomalies; the orange shadings show the results for the composites of the four warm years (Mean_{warm}) and cold years (Mean_{cold}).

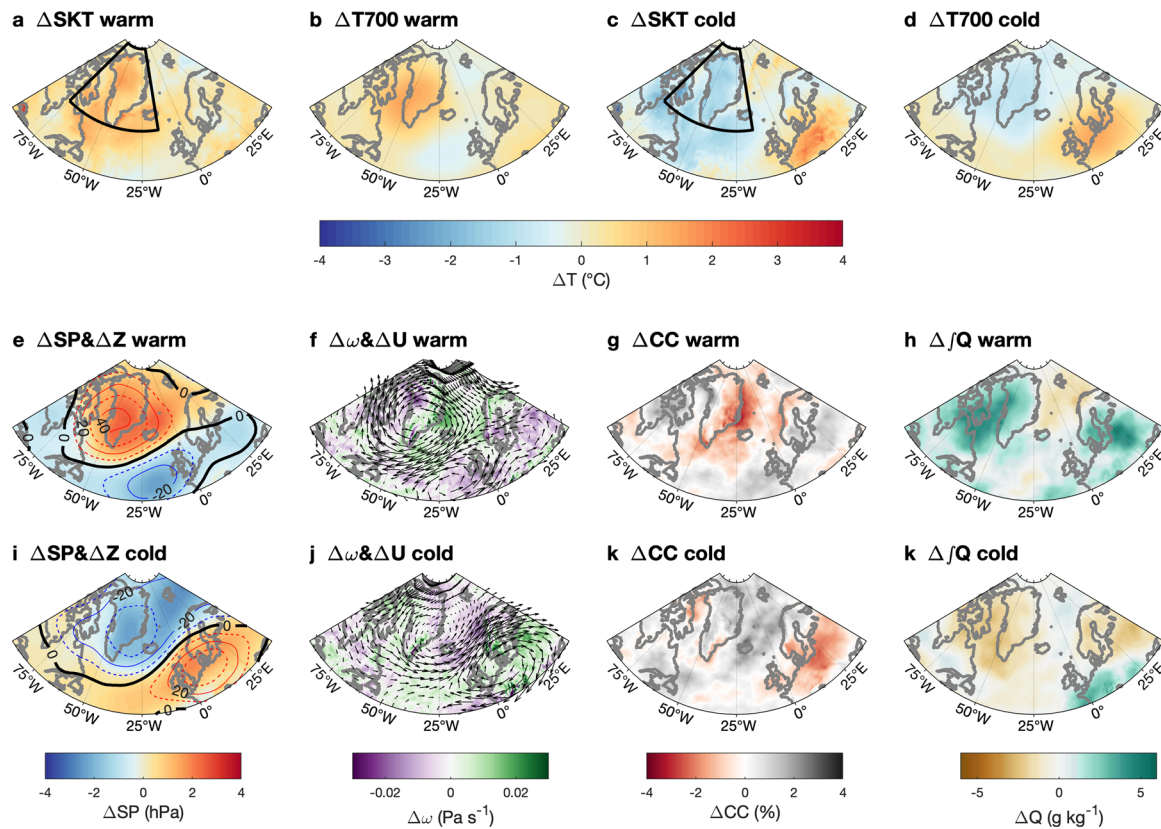


Fig. 2 | Composite atmospheric anomalies in extreme anomaly summers. The figure shows composite mean anomalies in the atmosphere characterizing warm and cold temperature years. The first row depicts the surface temperature (SKT) and 700 hPa temperature anomalies (T700) in warm anomaly years (a) and (b) and cold anomaly years (c) and (d), respectively. Anomalies in the surface pressure (shading; SP) and the geopotential height at 500 hPa (contours; Z) are shown in (e) and (i).

f and j Demonstrate anomalous vertical (shading; ω) and horizontal (vectors; U) circulation, g and k illustrate the anomalies in cloud cover (CC), and h and l vertically integrated specific humidity (Q). The second row presents the composite mean anomalies for the warm extreme years; the third row presents the composite mean anomalies for the cold extreme years. The black boxes in a and c outline the Greenland domain used for the mean value calculation.

that emerges, for instance, from perturbations in water vapor^{26,27,29,56}. The cloud radiative effect comprises the response of shortwave and longwave radiation due to changing cloud top height, optical depth, and phase. The non-radiative feedback processes include the effect of the net energy flux stored at the surface (HSTOR) and the effect of turbulent heat fluxes (HFLUX) on surface temperature perturbations²⁹. Here, surface temperature refers to the surface skin temperature. The surface temperature trends exhibit a distinct seasonality characterized by the minimum during summer (0.04 K yr^{-1}) and the maximum in winter (0.07 K yr^{-1})^{18,27,29}, all of which are statistically significant (based on a Mann–Kendall test with a 95% confidence interval).

Figure 1a indicates the dominant role of the surface albedo feedback and the perturbations in the clear-sky longwave radiation in shaping the warming trends. The effect of these two radiative contributions may play in tandem; increased warming hastens ice sheet degradation, which lowers surface albedo^{18,27} and, at the same time, may contribute to enhanced turbulent heat release⁵⁷. In contrast, other terms counteract the overall warming trend over Greenland (Fig. 1a).

Detrending shows that the clear-sky downwelling longwave radiation is the principal factor shaping interannual variability in Greenland surface temperature during summer (Fig. 1b). Both the clear-sky downwelling longwave radiation and the surface albedo feedback positively correlate with surface temperature. A near cancellation is observed between the cloud radiative effect and the surface albedo feedback over the regions²⁹, where thinning and ablating over the ice sheet in low-lying regions decreases snow and ice cover^{5,9,15}. These characteristics suggest the importance of atmospheric processes in determining clear-sky longwave radiation.

The detrended timeseries shown in Fig. 1b indicate that Greenland has experienced substantial interannual temperature anomalies in recent decades. Above-normal warm years include 1980, 2003, 2010, and 2012. In the latter years, unprecedented high temperatures occurred, accompanied by enhanced snowmelt rates^{6,7,25,55}. Cold years include 1983, 1992, 2015, and 2018 (Fig. 1c). Extracting the climate trend revealed the most recent cold year, 2018, to have cold anomalies of -0.89°C , the lowest temperature after 1992 with -1.34°C . The most recent warm anomaly year, 2012, remained unprecedentedly warm at 1.13°C . On average, the composite mean value of the cold years, -0.96°C , is more accentuated than the mean value of warm years, 0.81°C .

There are extreme warm and cold temperature anomalies in all eight cases. In both warm and cold years, detrended temperature anomalies around the Greenland domain are within the 10th percentile (Supplementary Fig. 2). The distinct positive surface temperature departures over the Ocean and major parts of Greenland characterize the warm extreme years. The significant cold anomalies span Greenland and the adjacent regions with stronger intensity. Further, the temperature anomalies at 700 hPa mimic the spatial pattern of the surface temperature anomalies. The detrended temperature anomaly timeseries over Greenland show a significant correlation between surface and 700 hPa air temperature anomalies over the surrounding ocean extending westwards towards Northeast Canada (Supplementary Fig. 1).

In the warm years, positive temperature anomalies were related to the combined contribution of the surface albedo feedback and the effect of perturbed downwelling clear-sky longwave radiation (Fig. 1c). Their combined impacts exceed the opposing impacts from the cloud radiative effect, the surface heat storage, and the turbulent heat flux, resulting in positive

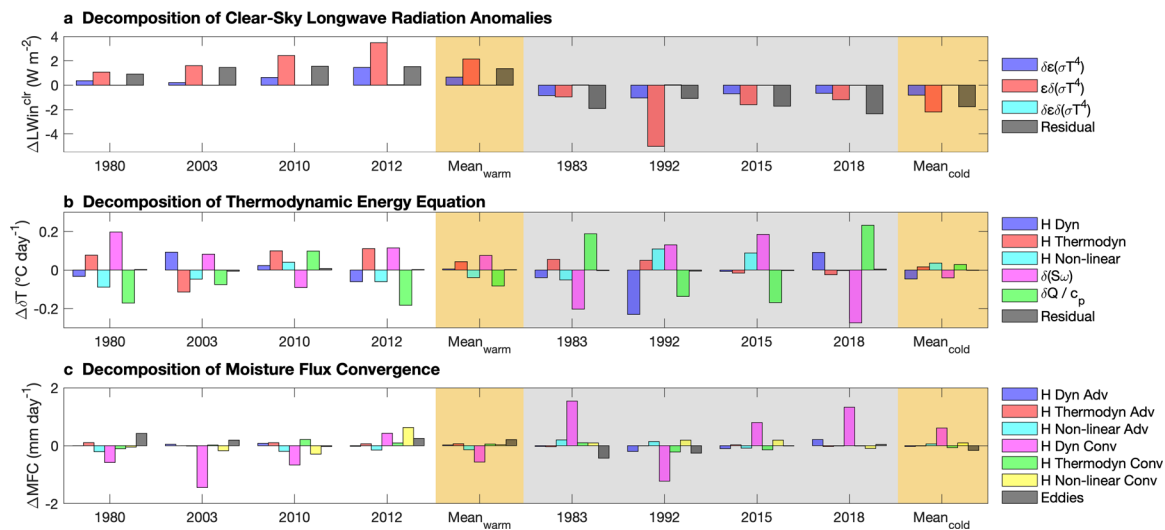


Fig. 3 | Decomposition of clear-sky downwelling longwave radiation, thermodynamic energy equation, and moisture flux convergence. The figure presents the results of the decomposition analysis of the clear-sky downwelling radiation (a), of the thermodynamic energy equation (b), and the moisture flux convergence (c) for

warm and cold years. The gray shading highlights the below-normal temperature anomalies; the orange shadings show the results for the composites of the four warm years (Mean_{warm}) and cold years (Mean_{cold}). Presented are summer mean values from a detrended timeseries.

temperature anomalies. Similarly, in the cold years, the surface energy budget perturbations are due to surface albedo feedback and the effect of clear-sky downwelling longwave radiation, counteracted by the changes in the heat storage term. The latter exerts a greater influence in the cold years compared to warm years. In both cases, the heat storage effect is the strongest opposing term to the heating or cooling. This agrees with the spatial correlation pattern between detrended Greenland temperature anomalies and the different terms contributing to the anomalous surface energy budget (Supplementary Fig. 1). A significant positive correlation between the Greenland surface temperature anomalies and the temperature effect of clear-sky longwave radiation is observed over the entire north-western Atlantic up to the coast of Europe (Supplementary Fig. 1f). There is large variability in the surface albedo feedback term, leaving the effect of downwelling clear-sky longwave radiation the principal contributor to temperature anomalies (Fig. 1), which is robust among different reanalysis products (Supplementary Fig. 3a).

Considering the perturbation in clear-sky downwelling longwave radiation was the dominant driver for surface temperature trends and anomalies over Greenland, one vital question emerges: what causes the perturbations of clear-sky downwelling longwave radiation? The clear-sky downwelling longwave radiation combines the effect of greenhouse gases and the atmospheric conditions^{26,27,29}. To explain the radiation anomalies, we decompose the clear-sky downwelling longwave radiation based on the Stefan–Boltzmann law into the component due to anomalies of atmospheric emissivity, the component due to anomalies of mean atmospheric temperature, and the non-linear term⁵⁸. This was done by applying a conceptual framework⁵⁸ with the idealized assumption of an isothermal atmosphere with homogenous gas distribution, which may be the source of uncertainty (see the “Methods” section). Both changes in the atmospheric mean temperature and the emissivity contribute to clear-sky longwave radiation anomalies with the same sign, while the nonlinear term is negligible. In conclusion, air temperature changes contribute more to the change in clear-sky longwave radiation, while emissivity changes play a secondary role (Fig. 3a). This is a robust finding in the different reanalysis products (Supplementary Fig. 3b).

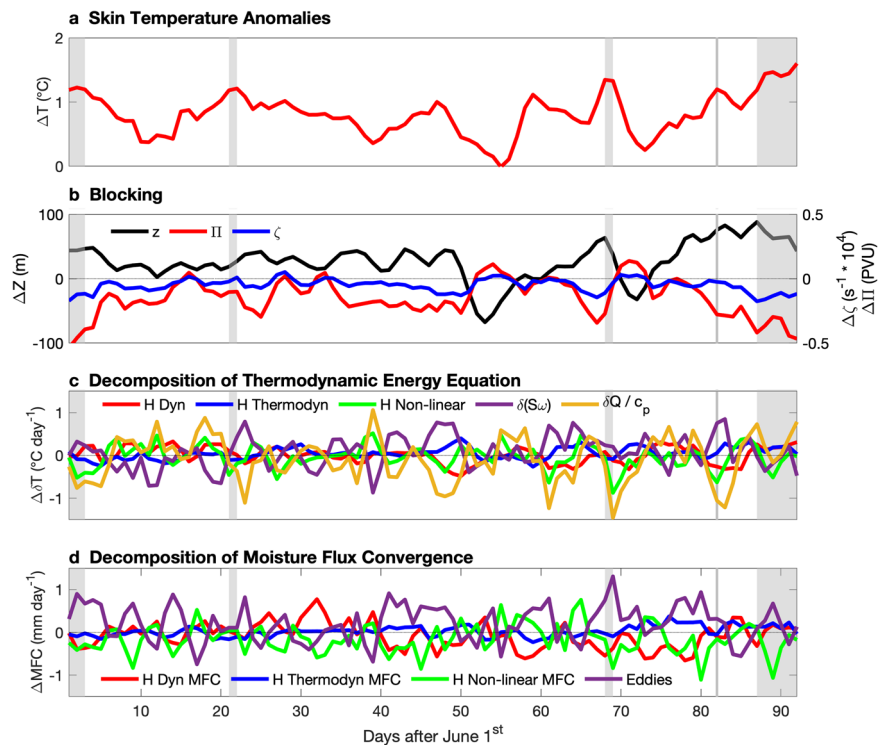
Considering the surface energy balance explains the temperature anomalies at the surface, we decomposed the thermodynamic energy equation^{58–61} to infer the underlying processes for anomalous air temperature tendencies over Greenland (Fig. 3b). Here, the focus is the anomalous atmospheric temperature at the 700 hPa pressure surface as it correlated well

with surface conditions and melting rates of the Greenland ice sheet^{3,8}. Therefore, the atmospheric temperature at 700 hPa can potentially demonstrate the linkage between Greenland summit surface conditions and large-scale circulation. The analysis demonstrates a strong contribution of adiabatic and diabatic temperature changes to anomalous temperature tendencies. Horizontal temperature advection often takes a subordinate role (Fig. 3b). Thermodynamic and dynamic processes impact the temperature tendency with opposing signs. Further, horizontal temperature advection shows distinct differences between warm and cold years. In warm years, thermodynamic processes induce positive temperature tendencies while dynamic contribution is negligible. In contrast, during cold years, dynamic changes in temperature advection induce strong cold anomalies, while thermodynamic processes play a minor role. In terms of horizontal temperature advection, there is a zonal gradient. The thermodynamic (non-linear) processes exert negative temperature tendencies over East (West) Greenland, which remains in both warm and cold years. In contrast, the dynamic processes result in negative temperature tendencies over East Greenland and positive tendencies in West Greenland in warm years and vice versa in cold years (Supplementary Fig. 4). This aligns with atmospheric anomalies in respective years (Fig. 2 and Supplementary Fig. 5). In warm years, strong anti-cyclonic anomalies enhance southward cold air advection east of Greenland; however, warm air propagates northward over Canada and the Labrador Strait. The center of this anomalous circulation pattern is located south of the Greenland summit (Fig. 2).

Except for 2003, changes in the horizontal temperature advection due to thermodynamic processes are positive or near zero; however, they have a weak magnitude in cold years. Over Greenland, the effect of thermodynamic processes is heterogeneously distributed (Supplementary Fig. 4). There is a strong signal over the northern coastal region of Greenland, where also surface temperature anomalies were most distinct in cold years, which leads to the assumption that the downward-sloping winds at the northern edge of the anti-cyclone heat up, warming the temperature at the surface and the atmosphere (Fig. 2). This warming effect could reach into the mid-troposphere¹³ and had a dominant effect on temperature anomalies and amplified ice melt rates on the northern coast of Greenland¹².

Adiabatic and diabatic heating are the dominant factors inducing anomalous temperature tendencies in warm and cold years. There is a pronounced positive adiabatic and negative diabatic term in both mean values and spatial patterns in warm years. These opposing effects also emerge from their spatial distribution over Greenland. While diabatic effects

Fig. 4 | Composite mean daily timeseries of anomalies in extreme warm temperature years. The figure presents the composite daily temperature anomalies timeseries in the four warm extreme years (a). Further, b illustrates the indicators for atmospheric blocking conditions (geopotential height anomalies, potential and relative vorticity anomalies). The daily results of the decomposed thermodynamic equation and the moisture flux convergence are included in (c) and (d). The gray shading shows positive peak temperature anomalies. The x-axis counts the days from June 1.



partly balance adiabatic heating, in sum, warming due to adiabatic heating is stronger in summer. In winter, the adiabatic heating term has a negative sign. In warm years, there is a strong adiabatic heating term contribution featuring strong positive values over southern and eastern parts of Greenland, while its values are negative over north and northwestern Greenland. The spatial pattern of the diabatic term mirrors that of the adiabatic term with opposite signs. The sign of the temperature tendency follows the adiabatic heating term due to its stronger effect on total anomalous temperature tendency (Fig. 3 and Supplementary Fig. 4). Strong stratification due to the cold environment with reduced convective activity characterizes the Arctic atmosphere²⁶. In warm years, positive temperature anomalies in the lower atmosphere may weaken static stability via altered vertical temperature gradient. This may result in a stronger upward motion of warm air, enhancing the warming in the troposphere. The warming atmosphere emits more downwelling longwave radiation, enhancing surface warming. A ridge in the 500 hPa geopotential height and positive surface pressure anomalies accompany the warming, indicating conditions characteristic of atmospheric blocking. There is a similar anomaly pattern in cold years with opposing signs (Fig. 2 and Supplementary Fig. 5).

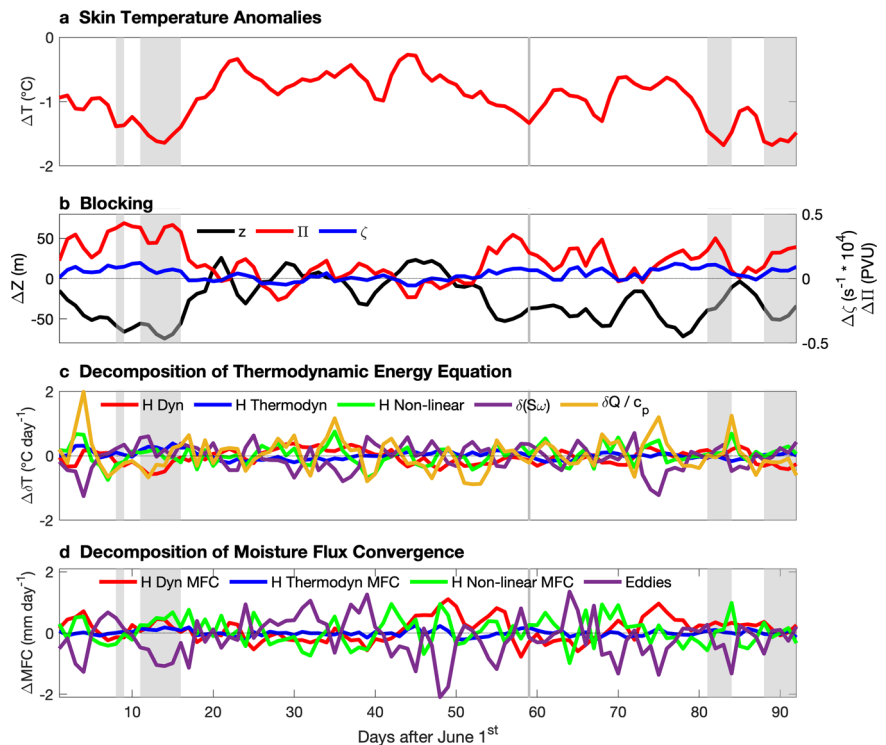
Even though the rate of clear-sky downwelling longwave radiation anomalies related to changes in emissivity is comparably small, particularly in cold years, it contributes a considerable part to the total perturbations (Fig. 3a). These anomalies result from the atmospheric chemical composition, such as the increase in water vapor in an anomalously warmer environment^{29,58,62}, which also acts as atmospheric feedback to enhance warming on a short timescale. To further elaborate on the cause of changing emissivity, we decomposed the moisture flux convergence into its dynamic, thermodynamic, and non-linear components of moisture advection and convergence and the effect of synoptic scale storm systems^{58,63} (see the “Methods” section). The dominance of dynamic anomalies to moisture flux convergence highlights the predominating role of circulation anomalies (Fig. 3c). Only in 2012 was a tandem of dynamical and non-linear moisture convergence attributed to the anomalous moisture flux convergence. Dynamic anomalies induce moisture divergence over Greenland, which coincides with a clearer sky in warm years. In contrast, the abundance of cloud cover results from moisture convergence due to enhanced circulation

anomalies. The center of the pressure, geopotential height, and cloud cover anomaly is located in the center of the anomalous circulation over the eastern coast of Greenland (Fig. 2 and Supplementary Figs. 5 and 6).

The causes of clear-sky downwelling longwave radiation perturbations can be determined by analyzing the thermodynamic energy equation and moisture flux convergence. Despite the negative seasonal mean values, diabatic warming is strong in the days before peak temperature anomalies in warm years (Fig. 4). Due to the thermal expansion, positive geopotential height anomalies follow those above-normal temperature days, indicating blocking. Negative anomalies in relative and potential vorticity accompany or follow peak temperature anomalies. Consequently, an anomalous anti-cyclonic circulation with subsidence with a core over east or southeast Greenland strengthens, leading to positive surface pressure anomalies and mid-troposphere geopotential height anomalies (Fig. 2). The anomalous anti-cyclone forces orographically induced ascending motion at the windward slopes of the Greenland topography and ice sheet in the northwest and southeast of Greenland and descending motion at the leeward slopes. At regions with orographic uplift, the negative adiabatic heating term prevails, while on the lee side, descending air warms. The slopes on the east coast are on the leeward side of the dominant background flow from the west. Here, the adiabatic heating is strongest, imposing a warming of the atmosphere and potentially an expansion of the inversion layer^{64,65}. As the surface temperature increases, snow and ice cover experience extensive melting^{64,65}, which causes a reduction of surface albedo, further warming the surface. Enhanced upward turbulent heat flux (Fig. 1c) can augment near-surface warming⁶⁵. There is a trend towards warmer temperatures and stronger adiabatic warming. An anti-cyclonic trend of the circulation forces orographic-induced vertical air movement in the proceeding days, which may weaken the atmospheric stability via an altered vertical temperature gradient (Fig. 2). The anomalous circulation triggers dynamic moisture convergence over Greenland, with the highest values at the coastal regions in the south and southwest (Figs. 2 and 4).

In cold years, a combination of horizontal temperature advection and diabatic heating, or adiabatic heating alone, determines the anomalous negative temperature tendency (Fig. 3). In the first case, an anomalous cyclone over Greenland explains the anomalous cold temperature tendency

Fig. 5 | Composite mean daily timeseries of anomalies in extremely cold temperature years. The figure presents the composite daily temperature anomalies timeseries in the four cold extreme years (a). Further, b illustrates the indicators for atmospheric blocking conditions (geopotential height anomalies, potential and relative vorticity anomalies). The daily results of the decomposed thermodynamic equation and the moisture flux convergence are included in (c) and (d). The gray shading shows negative peak temperature anomalies. The x-axis counts the days from June 1.



by northerly anomalies over parts of the west and interior Greenland (Supplementary Fig. 4g). Reduced blocking activity and cooler temperature allow the formation of clouds or fog (Fig. 2), reducing the surface temperature (Fig. 5). In the cooler atmosphere, there is reduced vertical velocity with ascending motion at windward slopes and descending motion at the leeward slopes. The negative dynamic term and adiabatic heating term imposed the negative anomalous temperature tendencies (Figs. 2 and 5).

The anomalous pressure and circulation patterns are similar in the warm and cold years, with opposite signs. In warm years, the maximum pressure anomalies are located near central Greenland southwest of the summit. The low is located over the British Isles (Fig. 2). Even though the ridge pattern is evident in each warm year, the spatial extent and exposition of the isolines may differ (Supplementary Fig. 5).

Prevailing blocking is an important characteristic of warm years, with increased frequency in summer months^{37–40,66}. The enhanced warming over the Arctic compared to lower latitudes weakened the westerlies and slowed Rossby waves⁶⁷. This could have led to increased waviness¹⁰ of the westerly jet and increased the probability of wave breaking⁶⁸, leading to a higher probability of blocking events⁴. Further, warming can favor stronger high-pressure and positive geopotential height anomaly conditions. Therefore, warming over Greenland may result in blocking-like trends of atmospheric variables, potentially increasing the occurrence of blocking over Greenland^{37,39,41}.

We quantified the contribution of various surface energy budget components to surface temperature anomalies over Greenland. The analysis demonstrates the importance of local processes, including diabatic and adiabatic warming, to the characteristics of extreme temperature summers over Greenland. It is important to stress that surface temperature has an upper limit of 273.15 K over snow and ice cover. When the temperature hits the freezing point, the excessive energy surplus contributes to melting and cooling the surface⁶⁹. This is particularly relevant for the heat storage term. To address this aspect, we partitioned the heat storage term according to surface conditions into contribution over ocean gridpoints (47.32%), land gridpoints (13.78%), snow and ice gridpoints (36.30%), and gridpoints in which snow starts to melt (2.60%). The heat storage term contributes the

strongest to surface temperature anomalies in ocean gridpoints (Supplementary Fig. 7a). The changes in the heat uptake or release of the ocean mainly determine the perturbations in the heat storage. During summer, the ice-free ocean can take a vast amount of energy as storage¹⁸. In particular, the anomalous vertical ocean heat transport correlated well with the partial temperature contributions of the heat storage term over ocean gridpoints (Supplementary Fig. 7). However, the exact determination of the role of ocean heat transport in temperature extremes is out of the scope of this study.

Natural variability

By analyzing the influence of climate indices on surface temperature anomalies, we put the regional temperature anomalies into a wider large-scale context^{32,35}. Anomalous high or low temperatures might be related to internal Arctic variability that could temporarily intensify or dampen long-term temperature trends. Four out of a set of 11 climate indices show significant Pearson's correlation, namely the North Atlantic Oscillation (NAO), the Greenland Blocking Index (GBI), the Arctic Oscillation (AO), and the Atlantic Multi-decadal Oscillation (AMO) (Supplementary Table 1).

There are reports of different climate modes interacting with each other. For instance, El Niño Southern Oscillation coupled with the Pacific decadal oscillation in their negative phase favored the development of strong negative Greenland blocking conditions and a positive North Atlantic oscillation^{34,70}. Others highlight the role of sea surface temperature, surface conditions, pressure, and geopotential height anomalies over the Pacific and North America to exert a remote influence on temperature anomalies over Greenland^{10,25,71}. Further, there is a high negative correlation between the Greenland blocking index and the North Atlantic Oscillation and other indices^{10,33,37,38} (Supplementary Table 1).

Considering the close relationship between some indices, the question of multi-collinearity emerges. Which index of the 11 indices is necessary to explain the surface temperature anomalies over Greenland? To address this question, first, we calculated partial correlation coefficients between each index and the surface temperature anomalies (Fig. 6a). Six indices share a significant partial correlation with the surface temperature anomalies,

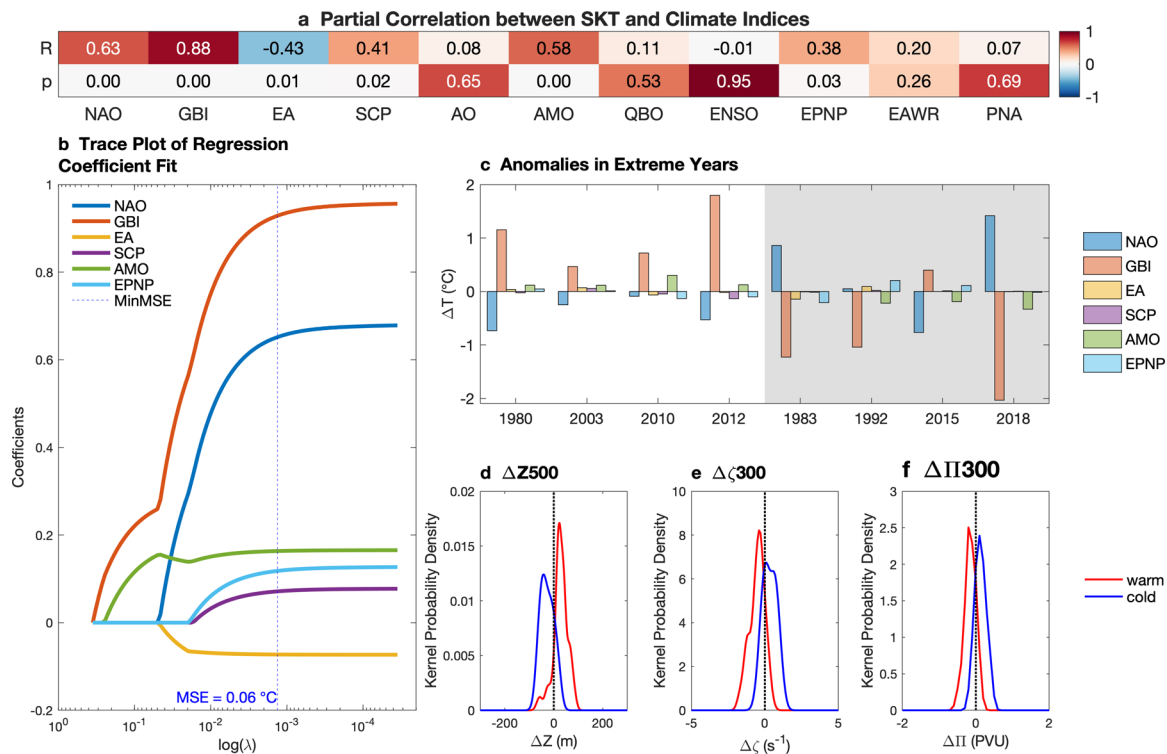


Fig. 6 | The role of natural variability to temperature tendencies over Greenland. The figure presents the relationship between surface temperature anomalies and different climate modes. The heatmap in **a** shows the partial correlation coefficients (R) and p -value statistics (p) between surface temperature and different indices of climate variability. **b** includes the trace plot presenting the fitting of the regression coefficients as part of the LASSO regression routine. The dotted blue line shows the lambda values generating the best fit with a mean square error of 0.06°C . The x -axis presents different lambda values on a logarithmic scale. Regressed surface temperature values in the selected extreme years are shown in **(c)**. Further, the Kernel probability densities of anomalies in the blocking indications are presented. Those

include the anomalies of 500 hPa geopotential height (**d**), 300 hPa relative vorticity (**e**), and 300 hPa potential vorticity (**f**), demonstrated for the daily composite mean anomalies of the four warm years (red) and the cold years (blue). In **a** and **b** the abbreviations refer to North Atlantic Oscillation (NAO), East Atlantic pattern (EA), Scandinavian Pattern (SCN), Greenland Blocking Index (GBI), Arctic Oscillation (AO), East Atlantic/West Russia pattern (EA/WR), East Pacific/North Pacific pattern (EP/NP), Pacific North America pattern (PNA), Quasi-Biennial Oscillation (QBO), El Niño Southern Oscillation index 3.4 (ENSO3.4), Atlantic Multi-decadal Oscillation (AMO).

including the North Atlantic oscillation (0.63), the Greenland blocking index (0.88), the East Atlantic pattern (-0.43), the Scandinavian pattern (0.41), the Atlantic multi-decadal oscillation (0.58), and the East Pacific/North Pacific pattern (0.38).

Second, we fitted a multivariate regression model using the lasso regression routine to quantify the contributions of all six indices (see the “Methods” section). The Greenland blocking index has the strongest correspondence with temperature anomalies, followed by the North Atlantic oscillation and the Atlantic multi-decadal oscillation (Fig. 6b). The resulting regressed surface temperature timeseries accurately captured the detrended surface temperature timeseries with a mean square error of 0.06°C . The lasso plot shows a two-level incline of regression coefficients for the Greenland blocking index (Fig. 6b). Significantly, the second increase of regression coefficients corresponds to the control factor (λ) at which the degree of freedom increases, and the other modes gain importance. At this point, the impact of the North Atlantic oscillation gains relevance for the regression model (Fig. 6b). Therefore, the effect of the Greenland blocking index and the North Atlantic oscillation cannot be considered in isolation but as an integrated part of the non-linear interplay of factors affecting Greenland warming. A negative phase of the North Atlantic oscillation and a positive Greenland blocking index combine the association with high-pressure conditions and anti-cyclonic circulation anomalies associated with blocking. Those features are characteristics of anomalously warm conditions over Greenland (Fig. 3 and Supplementary Fig. 5)^{6,9}. Further, the results of the lasso regression demonstrate, that sea surface temperature anomalies in the Atlantic Ocean contribute in part to the variability of Greenland temperature variability.

Summary and conclusion

We used a linear decomposition of the surface energy budget to explain surface temperature trends over Greenland in the ERA5 reanalysis data. In terms of linear trends, the effect of clear-sky downwelling longwave radiation was a dominant factor explaining the surface warming over Greenland. This warming trend was enhanced by the surface albedo feedback during summer, especially at the active ice margins and winter-time heat release from the ocean stored during summer months. In contrast, turbulent heat fluxes and the cloud radiative effect played an opposing role in Arctic surface warming, damping the effect of surface heating. This shows that local processes are important factors in explaining surface temperature anomalies over Greenland.

A physical mechanism was proposed to explain the pronounced temperature anomalies in anomalous warm and cold years. In warm years, diabatic heating triggers warm temperature anomalies, which can cause anomalies in the pressure and geopotential height and alter the vertical temperature gradient in the atmosphere. Further, anomalous circulation patterns develop over Greenland and the North Atlantic, with the center over the southeast of the Greenland summit. Consequently, an anomalous anti-cyclone forces ascending motion over the windward slopes in the west of Greenland, followed by reduced adiabatic warming. In contrast, the airflow descends along the leeward slopes along the east coast, inducing enhanced adiabatic warming. In the atmosphere, a positive anomaly of surface pressure and geopotential height and negative vorticity anomalies indicated a blocking feature characterized by an anomalous anti-cyclonic with subsidence over central Greenland and the eastern coast and ocean region. This causes moisture advection to Greenland from the south. This

triggered anomalous high clear-sky downward longwave radiation warming the surface. Due to surface warming, the snow and ice cover melted, leading to enhanced warming and turbulent heat release. This, in turn, increased the pressure and geopotential height anomalies, intensifying the anti-cyclonic anomalies. The mechanism occurred in cold years with the opposite sign.

Different indices describing modes of natural variability can help to explain temperature anomalies over Greenland. Based on the significant partial correlation, a multi-variate regression model containing the North Atlantic oscillation, the Greenland blocking index, the East Atlantic pattern, the Scandinavian pattern, the Atlantic multi-decadal oscillation, and the Pacific-North America pattern explained surface temperature anomalies over Greenland most accurately. The lasso regression showed that tandem of atmospheric anomalies, such as blocking and sea surface temperature anomalies in the Atlantic Ocean, explain the variability over Greenland, with the Greenland blocking index being the most relevant.

Methods

Data

We used the most recent output of the European Centre for Medium-Range Weather Forecasts (ECMWF) ERA5^{72–76}. We obtained monthly and hourly data for 00:00, 06:00, 12:00, and 18:00 and used the original grid for our analysis ($0.25^\circ \times 0.25^\circ$). Further, we used the data from the Japanese 55-year Reanalysis (JRA-55)^{77–79} on its original grid ($0.25^\circ \times 0.25^\circ$) and the reanalysis product of the National Center for Environmental Prediction and the National Center for Atmospheric Research (NCEP-NCAR)⁸⁰ on its original grid ($2.5^\circ \times 2.5^\circ$). We found robustness of the energy fluxes among the different reanalysis products (Supplementary Fig. 3a). Further, we used the Ocean Reanalysis System 5 (ORAS5)^{81,82}, which used ECMWF output as forcing, to estimate the ocean heat transport. We defined the Greenland domain as all gridpoints between 60°N and 85°N and between 15°W and 75°W .

Data processing

We analyzed monthly and hourly data (00, 06, 12, and 18 h). We used monthly data on their original grid; however, we interpolated hourly data from ERA5 and JRA55 to a $1^\circ \times 1^\circ$ grid. Further, we used the mean value of the boreal summer season—June, July, and August (JJA)—for the calculation. This study refers to detrended differences from the multi-year mean from 1979 to 2021 as anomalies. For resolving the anomalous moisture flux convergence and thermodynamic energy equation, anomalies refer to the difference in the actual values and the 6 hourly climatology.

Summer extreme temperature years

We selected extreme years by determining whether the detrended surface temperature anomaly in a given year exceeds a certain threshold. This threshold is based on the percentiles. Years with summer mean temperatures below the 10th percentile of the timeseries are characterized by below-normal (i.e., cold) extreme temperature summers, including 1983, 1992, 2015, and 2018. Years with summer mean temperatures above the 90th percentile are considered above-normal (i.e., warm) extreme temperature summers, including 1980, 2003, 2010, and 2012. The mean value of all above-normal and below-normal extreme temperature summers are considered as warm and cold composites, respectively.

Surface energy budget

To explain skin temperature anomalies, we used a linear energy budget decomposition method based on Lu and Cai²⁹. In this approach, we decomposed the total temperature anomaly into subcomponents associated with radiative and non-radiative perturbations. The sum of the partial temperature contributions (PTC) of all perturbations of energy and heat fluxes resulted in the total attributable temperature anomaly. This approach was widely used to analyze Arctic Amplification^{18,27,29} and was adapted by other studies, for example, to attribute elevation-dependent warming to the effects of surface energy budget perturbations⁵⁶.

The surface energy budget can be decomposed as follows²⁹:

$$Q = S^\downarrow - S^\uparrow + F^\downarrow - F^\uparrow - (H + L) \quad (1)$$

Q is the surface heat storage defined as the sum of downward shortwave radiation (S^\downarrow), upward shortwave radiation (S^\uparrow), downward longwave radiation (F^\downarrow), upward longwave radiation (F^\uparrow), sensible heat flux (H), and latent heat flux (L). The sign convention for the turbulent heat fluxes denotes downward energy fluxes with positive values.

Anomalies in the energy fluxes had an impact on Q and on the surface temperature. For anomalies in the surface heat storage and related energy fluxes, we rearranged Eq. (1) as²⁹

$$\Delta Q = \Delta S^\downarrow - \Delta S^\uparrow + \Delta F^\downarrow - \Delta F^\uparrow - \Delta(H + L), \quad (2)$$

$$4\sigma T_s^3 \Delta T = \Delta[(1 - \alpha)S^\downarrow] + \Delta F^\downarrow - \Delta Q - \Delta(H + L). \quad (3)$$

Here, Δ marks the change in the respective anomalies. Equation (2) was rearranged to relate ΔF^\uparrow , which can be expressed as $4\sigma T_s^3 \Delta T$, where σ is the Stefan-Boltzmann constant and T_s is the skin temperature (Eq. (3)).

The radiative effect of clouds on the surface energy budget needed further quantification. The approach used to derive cloud-related energy fluctuations followed the formulation described by Lu and Cai²⁹, relating anomalies in the longwave and shortwave radiation introduced by cloud anomalies,

$$\Delta \text{CRE} = (1 - \bar{\alpha})\Delta S^{\downarrow, \text{cld}} + \Delta F^{\downarrow, \text{cld}}. \quad (4)$$

Variables with cld as notation describe the difference between all-sky and clear-sky radiative fluxes^{27,29,56}.

Finally, we substituted the cloud effect—all cloud and cloud-related changes of shortwave and longwave radiation—into Eq. (4) and divided by $4\sigma T_s^3$. The resulting Eq. (5) gives the partial temperature contribution of the perturbations of the difference surface energy budget terms^{27,29,56}

$$\Delta T = \frac{-(\Delta\alpha)(\bar{S}^\downarrow + \Delta S^\downarrow) + \Delta \text{CRE} + (1 - \bar{\alpha})\Delta S^{\downarrow, \text{clr}} + \Delta F^{\downarrow, \text{clr}} - \Delta Q - \Delta(H + L)}{4\sigma T_s^3} \quad (5)$$

clr indicates the radiative energy fluxes under clear sky conditions. Equation (5) suggests the total skin temperature anomalies can be decomposed into the partial temperature contributions of six energy flux perturbations. Those include the effect of surface albedo feedback (SAF), the cloud radiative effect (CRE), the effect of anomalies in the clear-sky shortwave (SWCS) and downwelling longwave (LWCS) radiation, the effect of anomalies in the ocean and land heat storage (HSTOR), and the effect of anomalies in the surface turbulent heat flux (HFLUX). The heat storage combines the effect of net heat fluxes over land or ice, melt energy when the surface energy balance is positive and the temperature is 273.15 K, and over the ocean. On ocean gridpoints, the ocean heat transport adds or takes away energy. The first four terms describe the effect of radiative perturbations. The last two terms estimate the effect of non-radiative perturbations^{27,29,56}.

Change in clear-sky downwelling longwave radiation

We explained the changes in clear-sky downwelling longwave radiation by applying the Reynold decomposition to determine whether changes in emissivity, atmospheric mean temperature, or both components contribute more⁵⁸. The changes in clear-sky downwelling longwave radiation can be written as

$$\Delta F^{\downarrow, \text{clr}} = \Delta\epsilon[\sigma T_A^4] + \bar{\epsilon}\Delta[\sigma T_A^4] + \Delta\epsilon\Delta[\sigma T_A^4] - \Delta\epsilon\Delta[\sigma T_A^4]. \quad (6)$$

In Eq. (6), $F^{\downarrow, \text{dr}}$ is the clear-sky downwelling longwave radiation, ε is the emissivity, σ is the Stefan–Boltzmann constant, and T_A is the mean air temperature—the mean temperature between surface and 200 hPa. Δ denotes anomalies, and an overbar indicates the mean values. This is based on a conceptual model, assuming an isothermal atmosphere with homogeneous gas and water vapor distribution⁵⁸. Calculations of longwave radiation using the Stefan–Boltzmann law can inherit a source of uncertainty when applied to coarse time resolution⁸³. Radiative kernels, e.g., from Huang and Huang⁸⁴, can be used for a more accurate result. However, the differences are marginal.

We used the formulation of Fu and Liou⁸⁵ to calculate the downward emissivity of longwave radiation.

$$\varepsilon^{\downarrow} = \frac{F^{\downarrow}(z_b) - F^{\downarrow}(z_t)}{\sigma \bar{T}_A^4 - F^{\downarrow}(z_t)}, \quad (7)$$

where $F^{\downarrow}(z_b)$ is the downwelling radiation at the surface and $F^{\downarrow}(z_t)$ is the downwelling longwave radiation at the top of the atmosphere. In Eq. (7), $F^{\downarrow}(z_t)$ equals zero, while for $F^{\downarrow}(z_b)$, we used the clear-sky downwelling longwave radiation at the surface.

We used the temperature at 700 hPa as a reference to infer surface temperature anomalies and ice melt to large-scale circulation, as previously in Fettweis et al.^{3,8}. To explain temperature anomalies at 700 hPa, we used the thermodynamic energy equation following Clark and Feldstein⁵⁸

$$\frac{\partial T_A}{\partial t} = -u * \nabla T + S_p \omega + \frac{\dot{Q}}{c_p} + \text{Res} \quad (8)$$

$$S_p = -\left(\frac{T_A}{\theta}\right) * \left(\frac{\partial \theta}{\partial p}\right) \quad (9)$$

$$\dot{Q} = \frac{T_A}{\theta} * \left(\frac{\partial \theta}{\partial t} + \omega \frac{\partial \theta}{\partial p} + v_h * \nabla \theta\right) \quad (10)$$

$$\theta = T_A \left(\frac{p_s}{p}\right)^{\frac{R}{c_p}}, \quad (11)$$

Equation (8) expresses the temperature tendency per timestep with contributions of horizontal temperature advection, static stability, diabatic heating, and a residual term. We calculated static stability (S_p) with Eq. (9), where θ is the potential temperature, and p is pressure. Further, we used Eq. (10) to calculate diabatic heating⁸⁶, where ω denotes the vertical velocity. Equation (11) defines the potential temperature. p_s represents the surface pressure as the reference pressure. $R = (287 \text{ J kg}^{-1} \text{ K}^{-1})$ and $c_p = (1004 \text{ J kg}^{-1} \text{ K}^{-1})$ are the gas constant for dry air and the specific heat assuming constant pressure⁸⁷. In terms of anomalies, we can write Eq. (8) as

$$\begin{aligned} \frac{\partial T'}{\partial t} = & \left(-U' * \nabla \bar{T} + U' * \bar{\nabla} T'\right) + \left(-\bar{U} * \nabla T' + \bar{U} * \bar{\nabla} T'\right) \\ & + \left(-U' * \nabla T' + U' * \bar{\nabla} T'\right) + \left(-\bar{U} * \nabla \bar{T} + \bar{U} * \bar{\nabla} \bar{T}\right) \\ & + \left[S_p \omega\right]' + \left[\frac{\dot{Q}}{c_p}\right]' + \text{Res}' \end{aligned} \quad (12)$$

where variables indicated with prime are anomalies, and U is the wind velocity. The resulting expression describes the anomalous temperature tendency as a function of dynamic, thermodynamic, and non-linear terms of horizontal temperature advection, anomalous static stability, anomalous diabatic heating, and a residual term. Following this principle, we decomposed the anomalous moisture flux convergence into dynamic, thermodynamic, and non-linear terms of moisture advection and

convergence⁸⁸.

$$\begin{aligned} (P - E)' = & -\langle U' * \nabla \bar{q} \rangle - \langle \bar{q} * \nabla U' \rangle - \langle \bar{U} * \nabla q' \rangle - \langle q' * \nabla \bar{U} \rangle \\ & - \langle U' * \nabla q' \rangle - \langle q' * \nabla U' \rangle - \langle \nabla * (U' q') \rangle - \text{Residual} \end{aligned} \quad (13)$$

In Eq. (13), q is the specific humidity and $\langle \cdot \rangle$ denotes the mass-weighted vertical integration from 1000 to 200 hPa. The terms on the right-hand side read as changes in dynamic moisture convergence, dynamic moisture advection, thermodynamic moisture convergence, thermodynamic moisture advection, non-linear moisture convergence, non-linear moisture advection, the transient term, and a residual term. All were contributing to the total anomalous moisture flux convergence.

Ocean heat transfer

Finally, we used the ocean heat transfer^{89,90}

$$\text{OHF} = -\rho_0 c_p \int_{-H}^0 u \frac{\partial T}{\partial x} dz - \rho_0 c_p \int_{-H}^0 v \frac{\partial T}{\partial y} dz - \rho_0 c_p \int_{-H}^0 w \frac{\partial T}{\partial z} dz \quad (14)$$

where u, v, w , and z are the zonal, meridional, and vertical ocean currents and the depth of one layer, respectively. The heat advection of vertical motion was available in the ORAS5 database. We calculated the other terms. $\rho_0 c_p$ is the product of sea water density and heat capacity which Eq. (4) $1 \times 10^6 \text{ J m}^{-3} \text{ K}^{-1}$ ⁸⁹.

Climate Indices

We calculated 11 indices capturing different climate modes to relate Greenland temperature anomalies to large-scale circulation anomalies. All indices are based on the empirical orthogonal function (EOF) and the principal component analysis (PC) or absolute (anomaly) values. Table 1 lists details and definitions of the used climate indices. We used the indices as normalized timeseries.

LASSO regression

We used multivariate regression models to infer the effect of climate modes. A problem is the multi-collinearity—the significant correlation between the indices—which can decrease the robustness of the regression results. The least absolute shrinkage and selection operator (LASSO) regression^{91,92} routine offers an up-to-date tool to work around multi-collinearity in the indices and to avoid overfitting the regression model. The LASSO regression achieves this by reducing predictors and limiting the set of indices to the most relevant one. The concept can be written following Li et al.⁹³

$$\beta = \min_{\beta} \left\{ \sum_{i=1}^N (y_i - \hat{y}_i)^2 + \lambda \sum_{j=1}^p |\beta_j| \right\} \quad (15)$$

Here, λ is a control factor approaching 0 from the initial value of 1. Smaller λ increases the degree of freedom and more predictors contribute to the regression model. A λ approaching one constrains the regression model to the most relevant predictors. Cross-validation can be used to find the optimal λ for the regression model with minimum root mean square error^{92–94}.

Therefore, we used the lasso regression routine with a 10-fold cross-validation to form the multivariate regression model with minimum error⁹³.

Atmospheric blocking

The Greenland blocking index detected omega-blocking structures well due to their impact on geopotential height⁴¹. Several indices can detect blocking conditions in the North Atlantic and Greenland area considering both geopotential height and potential vorticity^{41,52,66,67}, for instance, a longer persisting negative potential vorticity anomaly⁵⁰.

Table 1 | Information on the climate modes used in this study

Index ^a	Domain		Variable ^b	Reference
	Longitude	Latitude		
NAO	90°W–40°E	20°–80°N	MSLP (PC1)	Hurrell ³⁴
EA			MSLP (PC2)	Barnston and Livezey ⁴²
				Comas-Bru and Hernández ⁴³
				Mellado-Cano et al. ⁴⁴
SCN			MSLP (PC3)	Comas-Bru and Hernández ⁴³
GBI	80°–20°W	60°–80°N	Z500	Hanna et al. ^{7,37,39}
AO	180°W–180°E	20°–90°N	Z1000 (PC1)	NOAA Climate Prediction Center ⁴⁵
EA/WR	180°W–180°E	15°–90°N	Z700 (PC2)	Barnston and Livezey ⁴²
EP/NP	180°W–180°E	15°–90°N	Z700 (PC4)	Barnston and Livezey ⁴²
PNA	NA = $\frac{1}{4} * [z * (20^{\circ}\text{N}, 160^{\circ}\text{W}) - z(45^{\circ}\text{N}, 165^{\circ}\text{W}) + z(55^{\circ}\text{N}, 115^{\circ}\text{W}) - z(30^{\circ}\text{N}, 85^{\circ}\text{W})]$		Z500	Wallace and Gutzler ⁴⁶
QBO	180°W–180°E	5°S–5°N	U50	Baldwin et al. ⁴⁷
ENSO3.4	170°W–120°W	5°S–5°N	SSTA	Barnston et al. ⁴⁸
AMO	80°W–0°E	0°N–60°N	SST	Trenberth and Shea ⁴⁹

^aNAO North Atlantic Oscillation, EA East Atlantic pattern, SCN Scandinavian Pattern, GBI Greenland Blocking Index, AO Arctic Oscillation, EA/WR East Atlantic/West Russia pattern, EP/NP East Pacific/North Pacific pattern, PNA Pacific North America pattern, QBO Quasi-Biennial Oscillation (QBO), ENSO3.4 El Niño Southern Oscillation index 3.4, AMO Atlantic Multi-decadal Oscillation.

^bMSLP mean sea level pressure, Z500 geopotential height at 500 hPa, Z700 at 700 hPa, and Z500 at 500 hPa pressure surface, U50 zonal wind component at 50 hPa, SSTA sea surface temperature/anomalies.

To explain differences between the effect of NAO and GBI, we used different indications of blocking, to determine the blocking strength and related heating related to the different modes of variability. Both negative relative and potential vorticity anomalies were associated with anti-cyclonic circulation and served as an indication of how blocking systems were structured. We calculated relative vorticity (ζ) and potential vorticity (Π) as⁸⁷

$$\zeta = \frac{\partial v}{\partial x} - \frac{\partial u}{\partial y} \quad (16)$$

$$\Pi = \frac{1}{\rho} \left(\frac{\partial v}{\partial x} - \frac{\partial u}{\partial y} + f \right) \frac{\partial \theta}{\partial z} \quad (17)$$

In Eq. (16), ∂v and ∂u are the gradients of the v -component and u -component of the wind vector, and ∂x and ∂y are the distance along the longitudes and latitudes, respectively. Potential vorticity is calculated using an approximation where f is the Coriolis force, ρ is the air density, and $\partial \theta / \partial z$ is the vertical gradient of potential temperature (θ)⁸⁷.

Data availability

The reanalysis output of “ERA5 monthly averaged data on single levels from 1940 to present” are available under the link <https://cds.climate.copernicus.eu/cdsapp#!/dataset/reanalysis-era5-single-levels-monthly-means?tab=overview> (last accessed 21/11/2023). The reanalysis output of “ERA5 monthly averaged data on pressure levels from 1940 to present” are available under the link <https://cds.climate.copernicus.eu/cdsapp#!/dataset/reanalysis-era5-pressure-levels-monthly-means?tab=overview> (last accessed 21/11/2023). The reanalysis output of “ERA5 hourly data on single levels from 1940 to present” are available under the link <https://cds.climate.copernicus.eu/cdsapp#!/dataset/reanalysis-era5-single-levels?tab=overview> (last accessed 21/11/2023). The reanalysis output of “ERA5 hourly data on pressure levels from 1940 to present” are available under the link <https://cds.climate.copernicus.eu/cdsapp#!/dataset/reanalysis-era5-pressure-levels?tab=overview> (last accessed 21/11/2023). The reanalysis output of “ORAS5 global ocean reanalysis monthly data from 1958 to present” are available under the link <https://cds.climate.copernicus.eu/cdsapp#!/dataset/reanalysis-oras5?tab=overview> (last accessed 21/11/2023). The reanalysis output of “JRA-55: Japanese 55-year Reanalysis, Monthly Means and Variances” are available under the link <https://rda.ucar.edu/datasets/ds628.1/> (last accessed 21/11/2023). The reanalysis output of “JRA-55: Japanese 55-year Reanalysis, Daily

3-Hourly and 6-Hourly Data” are available under the link <https://rda.ucar.edu/datasets/ds628.0/> (last accessed 21/11/2023). The reanalysis output of “NCEP-NCAR Reanalysis 1” are available under the link <https://psl.noaa.gov/data/gridded/data.ncep.reanalysis.html> (last accessed 21/11/2023).

Received: 6 December 2023; Accepted: 1 July 2024;

Published online: 28 July 2024

References

- Blau, M. T., Turton, J. V., Sauter, T. & Mölg, T. Surface mass balance and energy balance of the 79N Glacier (Nioghalvfjærdsfjorden, NE Greenland) modeled by linking COSIPY and Polar WRF. *J. Glaciol.* **67**, 1093–1107 (2021).
- Turton, J. V., Hochreuther, P., Reimann, N. & Blau, M. T. The distribution and evolution of supraglacial lakes on 79°N Glacier (north-eastern Greenland) and interannual climatic controls. *Cryosphere* **15**, 3877–3896 (2021).
- Fettweis, X., Mabilhe, G., Erpicum, M., Nicolay, S. & van den Broeke, M. The 1958–2009 Greenland ice sheet surface melt and the mid-tropospheric atmospheric circulation. *Clim. Dyn.* **36**, 139–159 (2011).
- Tedesco, M. et al. Arctic cut-off high drives the poleward shift of a new Greenland melting record. *Nat. Commun.* **7**, 11723 (2016).
- Fettweis, X., Tedesco, M., Van Den Broeke, M. & Ettema, J. Melting trends over the Greenland ice sheet (1958–2009) from spaceborne microwave data and regional climate models. *Cryosphere* **5**, 359–375 (2011).
- Tedesco, M. et al. Evidence and analysis of 2012 Greenland records from spaceborne observations, a regional climate model and reanalysis data. *Cryosphere* **7**, 615–630 (2013).
- Hanna, E. et al. Atmospheric and oceanic climate forcing of the exceptional Greenland ice sheet surface melt in summer 2012. *Int. J. Climatol.* **34**, 1022–1037 (2014).
- Fettweis, X. et al. Brief communication Important role of the mid-tropospheric atmospheric circulation in the recent surface melt increase over the Greenland ice sheet. *Cryosphere* **7**, 241–248 (2013).
- Tedesco, M. & Fettweis, X. Unprecedented atmospheric conditions (1948–2019) drive the 2019 exceptional melting season over the Greenland ice sheet. *Cryosphere* **14**, 1209–1223 (2020).
- Preece, J. R. et al. Summer atmospheric circulation over Greenland in response to Arctic amplification and diminished spring snow cover. *Nat. Commun.* **14**, 3759 (2023).

11. Gjelstrup, C. V. B. et al. Vertical redistribution of principle water masses on the Northeast Greenland Shelf. *Nat. Commun.* **13**, 7660 (2022).
12. Slater, D. A. & Straneo, F. Submarine melting of glaciers in Greenland amplified by atmospheric warming. *Nat. Geosci.* **15**, 794–799 (2022).
13. Mattingly, K. S. et al. Increasing extreme melt in northeast Greenland linked to foehn winds and atmospheric rivers. *Nat. Commun.* **14**, 1743 (2023).
14. Khan, S. A. et al. Sustained mass loss of the northeast Greenland ice sheet triggered by regional warming. *Nat. Clim. Chang.* **4**, 292–299 (2014).
15. Fettweis, X. et al. Reconstructions of the 1900–2015 Greenland ice sheet surface mass balance using the regional climate MAR model. *Cryosphere* **11**, 1015–1033 (2017).
16. Pithan, F. & Mauritsen, T. Arctic amplification dominated by temperature feedbacks in contemporary climate models. *Nat. Geosci.* **7**, 181–184 (2014).
17. Stuecker, M. F. et al. Polar amplification dominated by local forcing and feedbacks. *Nat. Clim. Chang.* **8**, 1076–1081 (2018).
18. Chung, E. S. et al. Cold-season Arctic amplification driven by Arctic Ocean-mediated seasonal energy transfer. *Earth's Future* **9**, e2020EF001898 (2021).
19. Dethloff, K., Handorf, D., Jaiser, R., Rinke, A. & Klinghammer, P. Dynamical mechanisms of Arctic amplification. *Ann. N. Y. Acad. Sci.* **1436**, 184–194 (2019).
20. Rantanen, M. et al. The Arctic has warmed nearly four times faster than the globe since 1979. *Commun. Earth Environ.* **3**, 168 (2022).
21. Dai, A., Luo, D., Song, M. & Liu, J. Arctic amplification is caused by sea-ice loss under increasing CO₂. *Nat. Commun.* **10**, 121 (2019).
22. Ryan, J. C. et al. Decreasing surface albedo signifies a growing importance of clouds for Greenland Ice Sheet meltwater production. *Nat. Commun.* **13**, 11723 (2022).
23. Janoski, T. P., Previdi, M., Chiodo, G., Smith, K. L. & Polvani, L. M. Ultrafast Arctic amplification and its governing mechanisms. *Environ. Res.: Clim.* **2**, 035009 (2023).
24. Hörhold, M. et al. Modern temperatures in central–north Greenland warmest in past millennium. *Nature* **613**, 503–507 (2023).
25. Matsumura, S., Yamazaki, K. & Suzuki, K. Slow-down in summer warming over Greenland in the past decade linked to central Pacific El Niño. *Commun. Earth Environ.* **2**, 257 (2021).
26. Goosse, H. et al. Quantifying climate feedbacks in polar regions. *Nat. Commun.* **9**, 1919 (2018).
27. Boeke, R. C. & Taylor, P. C. Seasonal energy exchange in sea ice retreat regions contributes to differences in projected Arctic warming. *Nat. Commun.* **9**, 5017 (2018).
28. Lu, J. & Cai, M. Quantifying contributions to polar warming amplification in an idealized coupled general circulation model. *Clim. Dyn.* **34**, 669–687 (2010).
29. Lu, J. & Cai, M. Seasonality of polar surface warming amplification in climate simulations. *Geophys. Res. Lett.* **36**, L16704 (2009).
30. Taylor, P. C. et al. A decomposition of feedback contributions to polar warming amplification. *J. Clim.* **26**, 7023–7043 (2013).
31. Jahfer, S. et al. Decoupling of Arctic variability from the North Pacific in a warmer climate. *NPJ Clim. Atmos. Sci.* **6**, 154 (2023).
32. Fettweis, X. Reconstruction of the 1979–2006 Greenland ice sheet surface mass balance using the regional climate model MAR. *Cryosphere* **1**, 21–40 (2007).
33. Davini, P., Cagnazzo, C., Neale, R. & Tribbia, J. Coupling between Greenland blocking and the North Atlantic Oscillation pattern. *Geophys. Res. Lett.* **39**, L14701 (2012).
34. Hurrell, J. W. Decadal trends in the North Atlantic oscillation: Regional temperatures and precipitation. *Science* (1979) **269**, 676–679 (1995).
35. Lim, Y. K. et al. Atmospheric summer teleconnections and Greenland Ice Sheet surface mass variations: insights from MERRA-2. *Environ. Res. Lett.* **11**, 024002 (2016).
36. Herein, M., Márffy, J., Drótos, G. & Tél, T. Probabilistic concepts in intermediate-complexity climate models: a snapshot attractor picture. *J. Clim.* **29**, 259–272 (2016).
37. Hanna, E., Cropper, T. E., Hall, R. J. & Cappelen, J. Greenland Blocking Index 1851–2015: a regional climate change signal. *Int. J. Climatol.* **36**, 4847–4861 (2016).
38. Hanna, E., Cropper, T. E., Jones, P. D., Scaife, A. A. & Allan, R. Recent seasonal asymmetric changes in the NAO (a marked summer decline and increased winter variability) and associated changes in the AO and Greenland Blocking Index. *Int. J. Climatol.* **35**, 2540–2554 (2015).
39. Hanna, E., Cropper, T. E., Hall, R. J., Cornes, R. C. & Barriendos, M. Extended North Atlantic Oscillation and Greenland Blocking Indices 1800–2020 from New Meteorological Reanalysis. *Atmosphere (Basel)* **13**, 436 (2022).
40. Chan, P. W., Catto, J. L. & Collins, M. Heatwave–blocking relation change likely dominates over decrease in blocking frequency under global warming. *NPJ Clim. Atmos. Sci.* **5**, 68 (2022).
41. Preece, J. R., Wachowicz, L. J., Mote, T. L., Tedesco, M. & Fettweis, X. Summer Greenland blocking diversity and its impact on the surface mass balance of the Greenland ice sheet. *J. Geophys. Res.: Atmos.* **127**, e2021JD035489 (2022).
42. Barnston, A. G. & Livezey, R. E. Classification, seasonality and persistence of low-frequency atmospheric circulation patterns. *Mon. Weather Rev.* **115**, 1083–1126 (1987).
43. Comas-Bru, L. & Hernández, A. Reconciling North Atlantic climate modes: revised monthly indices for the East Atlantic and the Scandinavian patterns beyond the 20th century. *Earth Syst. Sci. Data* **10**, 2329–2344 (2018).
44. Mellado-Cano, J., Barriopedro, D., García-Herrera, R., Trigo, R. M. & Hernández, A. Examining the north Atlantic oscillation, east Atlantic pattern, and jet variability since 1685. *J. Clim.* **32**, 6285–6298 (2019).
45. NOAA Climate Prediction Center. *Teleconnection Pattern Calculation Procedures. 1. Arctic/Antarctic Oscillation (AO/AO)* https://www.cpc.ncep.noaa.gov/products/precip/CWlink/daily_ao_index/history/method.shtml (NOAA Climate Prediction Center, 2005).
46. Wallace, J. M. & Gutzler, D. S. Teleconnections in the geopotential height field during the Northern Hemisphere winter. *Mon. Weather Rev.* **109**, 784–812 (1981).
47. Baldwin, M. P. et al. The quasi-biennial oscillation. *Rev. Geophys.* **39**, 179–229 (2001).
48. Barnston, A. G., Chelliah, M. & Goldenberg, S. B. Documentation of a highly enso-related sst region in the equatorial pacific: research note. *Atmosphere—Ocean* **35**, 367–383 (1997).
49. Trenberth, K. E. & Shea, D. J. Atlantic hurricanes and natural variability in 2005. *Geophys. Res. Lett.* **33**, L12704 (2006).
50. Kautz, L. A. et al. Atmospheric blocking and weather extremes over the Euro-Atlantic sector—a review. *Weather Clim. Dyn.* **3**, 305–336 (2022).
51. Barrett, B. S., Henderson, G. R., McDonnell, E., Henry, M. & Mote, T. Extreme Greenland blocking and high-latitude moisture transport. *Atmos. Sci. Lett.* **21**, e1002 (2020).
52. Sillmann, J. & Croci-Maspoli, M. Present and future atmospheric blocking and its impact on European mean and extreme climate. *Geophys. Res. Lett.* **36**, L10702 (2009).
53. Chan, P. W., Hassanzadeh, P. & Kuang, Z. Evaluating indices of blocking anticyclones in terms of their linear relations with surface hot extremes. *Geophys. Res. Lett.* **46**, 4904–4912 (2019).
54. Yao, Y. & De-Hai, L. The anomalous European climates linked to different Euro-Atlantic blocking. *Atmos. Ocean. Sci. Lett.* **7**, 309–313 (2014).
55. Andernach, M., Turton, J. V. & Mölg, T. Modeling cloud properties over the 79°N Glacier (Nioghalvfjærdsfjorden, NE Greenland) for an intense summer melt period in 2019. *Q. J. R. Meteorol. Soc.* **148**, 3566–3590 (2022).

56. Kad, P., Blau, M. T., Ha, K. & Zhu, J. Elevation-dependent temperature response in early Eocene using paleoclimate model experiment. *Environ. Res. Lett.* **17**, 114038 (2022).
57. Ford, T. W. & Frauenfeld, O. W. Surface–atmosphere moisture interactions in the frozen ground regions of Eurasia. *Sci. Rep.* **6**, 19163 (2016).
58. Clark, J. P. & Feldstein, S. B. What drives the North Atlantic oscillation’s temperature anomaly pattern? Part II: A decomposition of the surface downward longwave radiation anomalies. *J. Atmos. Sci.* **77**, 199–216 (2020).
59. Hsu, P. C. et al. East Antarctic cooling induced by decadal changes in Madden–Julian oscillation during austral summer. *Sci. Adv.* **7**, eabf9903 (2021).
60. Clark, J. P. & Feldstein, S. B. What drives the North Atlantic oscillation’s temperature anomaly pattern? Part I: The growth and decay of the surface air temperature anomalies. *J. Atmos. Sci.* **77**, 185–198 (2020).
61. Clark, J. P., Shenoy, V., Feldstein, S. B., Lee, S. & Goss, M. The role of horizontal temperature advection in arctic amplification. *J. Clim.* **34**, 2957–2976 (2021).
62. Kim, K. Y. et al. Vertical feedback mechanism of winter Arctic amplification and sea ice loss. *Sci. Rep.* **9**, 1184 (2019).
63. Jakobson, E. & Vihma, T. Atmospheric moisture budget in the Arctic based on the ERA-40 reanalysis. *Int. J. Climatol.* **30**, 2175–2194 (2010).
64. Woods, C., Caballero, R. & Svensson, G. Large-scale circulation associated with moisture intrusions into the Arctic during winter. *Geophys. Res. Lett.* **40**, 4717–4721 (2013).
65. Woods, C. & Caballero, R. The role of moist intrusions in winter Arctic warming and sea ice decline. *J. Clim.* **29**, 4473–4485 (2016).
66. Wachowicz, L. J., Preece, J. R., Mote, T. L., Barrett, B. S. & Henderson, G. R. Historical trends of seasonal Greenland blocking under different blocking metrics. *Int. J. Climatol.* **41**, E3263–E3278 (2021).
67. Luo, D., Chen, X., Dai, A. & Simmonds, I. Changes in atmospheric blocking circulations linked with winter Arctic warming: a new perspective. *J. Clim.* **31**, 7661–7678 (2018).
68. Franzke, C., Lee, S. & Feldstein, S. B. Is the North Atlantic Oscillation a breaking wave? *J. Atmos. Sci.* **61**, 145–160 (2004).
69. Mölg, T. & Hardy, D. R. Ablation and associated energy balance of a horizontal glacier surface on Kilimanjaro. *J. Geophys. Res. D: Atmos.* **109**, D16104 (2004).
70. Ding, S., Chen, W., Feng, J. & Grafa, H. F. Combined impacts of PDO and two types of La Niña on climate anomalies in Europe. *J. Clim.* **30**, 3253–3278 (2017).
71. Ibeuchi, C. C. & Lee, C. C. Circulation patterns associated with trends in summer temperature variability patterns in North America. *Sci. Rep.* **13**, 12536 (2023).
72. Hersbach, H. et al. The ERA5 global reanalysis. *Q. J. R. Meteorol. Soc.* **146**, 1999–2049 (2020).
73. Hersbach, H. et al. *ERA5 Monthly Averaged Data on Single Levels from 1940 to Present*. (Copernicus Climate Change Service (C3S) Climate Data Store (CDS), 2023).
74. Hersbach, H. et al. *ERA5 Monthly Averaged Data on Pressure Levels from 1940 to Present*. (Copernicus Climate Change Service (C3S) Climate Data Store (CDS), 2023).
75. Hersbach, H. et al. *ERA5 hourly Data on Single Levels from 1940 to Present*. (Copernicus Climate Change Service (C3S) Climate Data Store (CDS), 2023).
76. Hersbach, H. et al. *ERA5 Hourly Data on Pressure Levels from 1940 to Present*. (Copernicus Climate Change Service (C3S) Climate Data Store (CDS), 2023).
77. JRA-55: Japanese 55-year Reanalysis. *Monthly Means and Variances* (Japan Meteorological Agency, Research Data Archive at the National Center for Atmospheric Research, Computational and Information Systems Laboratory, 2013).
78. JRA-55: Japanese 55-year Reanalysis. *Daily 3-hourly and 6-hourly Data* (Japan Meteorological Agency, Research Data Archive at the National Center for Atmospheric Research, Computational and Information Systems Laboratory, 2013).
79. Kobayashi, S. et al. The JRA-55 reanalysis: general specifications and basic characteristics. *J. Meteorol. Soc. Jpn.* **93**, 5–48 (2015).
80. Kalnay, E. et al. The NCEP NCAR 40-year reanalysis project. *Bull. Am. Meteorol. Soc.* **77**, 437–472 (1996).
81. ORAS5. *Global Ocean Reanalysis Monthly Data from 1958 to Present* (Copernicus Climate Change Service (C3S) Climate Data Store (CDS), 2021).
82. Zuo, H., Balmaseda, M. A., Tietsche, S., Mogensen, K. & Mayer, M. The ECMWF operational ensemble reanalysis-analysis system for ocean and sea ice: a description of the system and assessment. *Ocean Sci.* **15**, 779–808 (2019).
83. An, N., Hemmati, S. & Cui, Y. J. Assessment of the methods for determining net radiation at different time-scales of meteorological variables. *J. Rock Mech. Geotech. Eng.* **9**, 239–246 (2017).
84. Huang, H. & Huang, Y. Radiative sensitivity quantified by a new set of radiation flux kernels based on the ECMWF Reanalysis v5 (ERA5). *Earth Syst. Sci. Data* **15**, 3001–3021 (2023).
85. Fu, Q. & Liou, K. N. Parameterization of the radiative properties of cirrus clouds. *J. Atmos. Sci.* **50**, 2008–2025 (1993).
86. Kad, P., Ha, K.-J., Lee, S.-S. & Chu, J.-E. Projected changes in mountain precipitation under CO₂-induced warmer climate. *Earth’s Future* **11**, e2023EF003886 (2023).
87. Holton, J. R. & Hakim, G. J. *An Introduction to Dynamic Meteorology*. (Elsevier, Oxford, Waltham, 2013).
88. Oh, H., Ha, K. J. & Timmermann, A. Disentangling impacts of dynamic and thermodynamic components on late summer rainfall anomalies in East Asia. *J. Geophys. Res.: Atmos.* **123**, 8623–8633 (2018).
89. DiNezio, P. N. et al. Climate response of the equatorial Pacific to global warming. *J. Clim.* **22**, 4873–4892 (2009).
90. Sharma, S. et al. Future Indian Ocean warming patterns. *Nat. Commun.* **14**, 1789 (2023).
91. Tibshirani, R. Regression shrinkage and selection via the Lasso. *J. R. Stat. Soc.: Ser. B (Methodological)* **58**, 267–288 (1996).
92. Ranstam, J. & Cook, J. A. LASSO regression. *Br. J. Surg.* **105**, 1348–1348 (2018).
93. Li, J., Pollinger, F. & Peath, H. Comparing the lasso predictor-selection and regression method with classical approaches of precipitation bias adjustment in decadal climate predictions. *Mon. Weather Rev.* **148**, 4339–4351 (2020).
94. Rachmawati, R. N., Sari, A. C. & Yohanes, L. Regression for daily rainfall modeling at Citeko Station, Bogor, Indonesia. *Procedia Comput. Sci.* **179**, 383–390 (2021).

Acknowledgements

M.T.B. and K.-J.H. were supported by the Institute for Basic Science (IBS), Republic of Korea, under the grant IBS-R028-D1. The research was further supported by the National Research Foundation of Korea (NRF) grant funded by the Korean government (MSIT), under the grant 2020R1A2C2006860. Additionally, K.-J.H. was supported by the Global–Learning & Academic research institution for Master’s, PhD students, and Postdocs (LAMP) Program of the National Research Foundation of Korea (NRF) grant funded by the Ministry of Education (No. RS-2023-00301938). E.-S.C. was supported by a Korea Polar Research Institute (KOPRI) grant funded by the Ministry of Oceans and Fisheries (KOPRI PE24010). We want to acknowledge the Climate Data Store (CDS) for providing ERA5 and ORAS5 datasets, the Research data archive of NCAR for providing JRA-55 datasets, and the Physical Sciences Laboratory from the National Oceanic and Atmospheric Administration (NOAA PSL) for providing NCEP-NCAR reanalysis 1 datasets. We acknowledge the support of KREONET.

Author contributions

M.T.B. and K.-J.H. designed this study. M.T.B. performed the investigation, produced the figures, and contributed to the initial draft and manuscript. K.-J.H. supervised this study, assisted in the investigation, discussed the results, and contributed to the draft and manuscript. E.-S.C. contributed to the draft and discussed the results. All authors interpreted the results and contributed to the manuscript.

Competing interests

The authors declare no competing interests.

Additional information

Supplementary information The online version contains supplementary material available at <https://doi.org/10.1038/s43247-024-01549-7>.

Correspondence and requests for materials should be addressed to Kyung-Ja Ha or Eui-Seok Chung.

Peer review information *Communications Earth & Environment* thanks the anonymous reviewers for their contribution to the peer review of this work. Primary Handling Editors: Sylvia Sullivan, Heike Langenberg, Alienor Lavergne. A peer review file is available

Reprints and permissions information is available at <http://www.nature.com/reprints>

Publisher's note Springer Nature remains neutral with regard to jurisdictional claims in published maps and institutional affiliations.

Open Access This article is licensed under a Creative Commons Attribution 4.0 International License, which permits use, sharing, adaptation, distribution and reproduction in any medium or format, as long as you give appropriate credit to the original author(s) and the source, provide a link to the Creative Commons licence, and indicate if changes were made. The images or other third party material in this article are included in the article's Creative Commons licence, unless indicated otherwise in a credit line to the material. If material is not included in the article's Creative Commons licence and your intended use is not permitted by statutory regulation or exceeds the permitted use, you will need to obtain permission directly from the copyright holder. To view a copy of this licence, visit <http://creativecommons.org/licenses/by/4.0/>.

© The Author(s) 2024